

Exploring negative ion behaviors and their influence on properties of DC magnetron sputtered ITO films under varied power and pressure conditions

Maoyang Li(李茂洋), Chaochao Mo(莫超超), Peiyu Ji(季佩宇), Xiaoman Zhang(张潇漫), Jiali Chen(陈佳丽), Lanjian Zhuge(诸葛兰剑), Xuemei Wu(吴雪梅), Haiyun Tan(谭海云), and Tianyuan Huang(黄天源)

Citation: Chin. Phys. B, 2024, 33 (**10**): 108102. DOI: 10.1088/1674-1056/ad62df
Journal homepage: http://cpb.iphy.ac.cn; http://iopscience.iop.org/cpb

What follows is a list of articles you may be interested in

Determination of band alignment between GaO_x and boron doped diamond for a selective-area-doped termination structure

Qi-Liang Wang(王启亮), Shi-Yang Fu(付诗洋), Si-Han He(何思翰), Hai-Bo Zhang(张海波),Shao-Heng Cheng(成绍恒), Liu-An Li(李柳暗), and Hong-Dong Li(李红东)
Chin. Phys. B, 2022, 31 (**8**): 088104. DOI: 10.1088/1674-1056/ac464e

Comparative study of high temperature anti-oxidation property of sputtering deposited stoichiometric and Si-rich SiC films

Hang-Hang Wang(王行行), Wen-Qi Lu(陆文琪), Jiao Zhang(张娇), and Jun Xu(徐军)
Chin. Phys. B, 2022, 31 (**4**): 048103. DOI: 10.1088/1674-1056/ac3a61

Structural and electrical properties of reactive magnetron sputtered yttrium-doped HfO_2 films

Yu Zhang(张昱), Jun Xu(徐军), Da-Yu Zhou(周大雨), Hang-Hang Wang(王行行), Wen-Qi Lu(陆文琪), Chi-Kyu Choi
Chin. Phys. B, 2018, 27 (**4**): 048103. DOI: 10.1088/1674-1056/27/4/048103

Rare earth Ce-modified (Ti,Ce)/a-C: H carbon-based filmon WC cemented carbide substrate

Shengguo Zhou(周升国), Zhengbing Liu(刘正兵), Shuncai Wang(王顺才)
Chin. Phys. B, 2017, 26 (**1**): 018101. DOI: 10.1088/1674-1056/26/1/018101

Field emission properties of a-C and a-C:H films deposited on silicon surfaces modified with nickel nanoparticles

Jin-Long Jiang(姜金龙), Yu-Bao Wang(王玉宝), Qiong Wang(王琼), Hao Huang(黄浩), Zhi-Qiang Wei(魏智强), Jun-Ying Hao(郝俊英)
Chin. Phys. B, 2016, 25 (**4**): 048101. DOI: 10.1088/1674-1056/25/4/048101

Exploring negative ion behaviors and their influence on properties of DC magnetron sputtered ITO films under varied power and pressure conditions

Maoyang Li(李茂洋)[1,3], Chaochao Mo(莫超超)[2], Peiyu Ji(季佩宇)[3,4], Xiaoman Zhang(张潇漫)[1,3], Jiali Chen(陈佳丽)[6], Lanjian Zhuge(诸葛兰剑)[5], Xuemei Wu(吴雪梅)[1,3], Haiyun Tan(谭海云)[1,3,‡], and Tianyuan Huang(黄天源)[1,3,†]

[1] *School of Physical Science and Technology, Soochow University, Suzhou* 215000, *China*
[2] *Suzhou Maxwell Technologies Co., Ltd., Suzhou* 215000, *China*
[3] *Jiangsu Key Laboratory of Frontier Material Physics and Devices, Suzhou* 215000, *China*
[4] *School of Optoelectronic Science and Engineering, Soochow University, Suzhou* 215000, *China*
[5] *Analysis and Testing Center, Soochow University, Suzhou* 215000, *China*
[6] *School of Optical and Electronic Information, Suzhou City University & Suzhou Key Laboratory of Biophotonics, Suzhou* 215104, *China*

(Received 10 May 2024; revised manuscript received 3 July 2024; accepted manuscript online 15 July 2024)

We deposited indium-tin-oxide (ITO) films on silicon and quartz substrates by magnetron sputtering technology in pure argon. Using electrostatic quadrupole plasma diagnostic technology, we investigate the effects of discharge power and discharge pressure on the ion flux and energy distribution function of incidence on the substrate surface, with special attention to the production of high-energy negative oxygen ions, and elucidate the mechanism behind its production. At the same time, the structure and properties of ITO films are systematically characterized to understand the potential effects of high energy oxygen ions on the growth of ITO films. Combining with the kinetic property analysis of sputtering damage mechanism of transparent conductive oxide (TCO) thin films, this study provides valuable physical understanding of optimization of TCO thin film deposition process.

Keywords: magnetron sputtering, ion energy, ITO thin film, high energy oxygen anion

PACS: 81.15.Cd, 52.70.–m, 61.80.Jh, 77.84.Bw **DOI:** 10.1088/1674-1056/ad62df

1. Introduction

Photovoltaic energy has increasingly emerged as a pivotal driver in the global energy structural transformation.[1] In comparison to traditional passivated emitter and rear cell (PERC) solar cells, heterojunction with intrinsic thin-film (HJT) heterojunction solar cells offer superior advantages, including enhanced conversion efficiency ($> 25\%$), minimal susceptibility to optical degradation, and a reduced temperature coefficient.[2,3] In the manufacturing process of HJT solar cells, it is essential to deposit a transparent conductive oxide (TCO) thin film on passivation surface to improve the lateral conductivity of the passivating hydrogenated amorphous silicon (a-Si:H) layer. Currently, the prevalent approach involves the utilization of direct current (DC) magnetron sputtering technology for TCO thin film deposition. Nevertheless, this deposition process gives rise to the issue of "sputtering damage", which diminishes the passivation quality of the a-Si:H layer and the optoelectronic performance of the TCO thin film.[4,5] The effective mitigation of sputtering damage is a focal concern within the photovoltaic industry, as it significantly impacts the conversion efficiency limit and yield in the mass production of HJT solar cells, thus representing one of the current industry's focal points of discussion.

The formation of sputtering damage constitutes a complex multiscale physical process encompassing sputtering, transport, and deposition across three distinct regions. Within the process of thin-film TCO deposition, a substantial population of negative ions (O^-, O_2^-, InO^-, among others) is generated near the target surface. These ions, possessing energies approaching the target voltage (on the order of hundreds of electron volts), collide with the substrate, resulting in sputtering and etching of the deposition layer. This phenomenon stands as the primary causative factor underlying the occurrence of sputtering damage in TCO thin films.[6–9] In the 1970s, the Palo Alto Research Center in the United States first confirmed that high-energy particle irradiation introduces structural defects within the a-Si:H deposition layer. It was postulated that ion-induced damage could potentially constitute the core issue affecting the efficiency of future HJT devices.[10] Subsequently, researchers at the AIFOKA Corporation in Japan observed a significant increase in the resistivity of indium-tin-oxide (ITO) thin films with elevated target voltage. This effect was attributed for the first time to crystalline damage resulting from the high-energy oxygen negative ions bombarding the thin film.[11] Researchers have demonstrated

†Corresponding author. E-mail: tyhuang@suda.edu.cn
‡Corresponding author. E-mail: hytan@suda.edu.cn
© 2024 Chinese Physical Society and IOP Publishing Ltd

that high-energy negative ions serve as a pivotal determinant in the extent of sputtering damage. No matter whether the objective is to diminish power or elevate gas pressure, the ultimate aim is to reduce the flux and energy of high-energy negative ions.[12,13]

Achieving comprehensive monitoring of high-energy negative ions throughout the TCO magnetron sputtering deposition process is a prerequisite for comprehending the physical mechanisms underlying sputtering damage and developing damage mitigation techniques. The evolution of energy-resolved mass spectrometry techniques has provided a robust means for diagnosing the behavior of high-energy negative ions. Tominaga *et al.* from Tokushima University, Japan, pioneered the direct measurement of high-energy negative ions during magnetron sputtering using an improved Faraday cup apparatus.[14] The development of energy-resolved mass spectrometry techniques has also facilitated diagnostic research on high-energy negative ions. For instance, in their investigation of the sputtering process of metal targets in argon/oxygen atmospheres, Mraz *et al.* discovered various negative ions predominantly composed of O^- ions, whose energies matched the target voltage, confirming the origin of high-energy negative ions from the target surface.[15] Welzel *et al.* systematically analyzed the lateral distribution of oxygen negative ions incident on the substrate surface, confirming the highest flux of high-energy oxygen negative ions in the groove region of the target surface.[16] Although these studies investigated the influence of plasma parameters on ion energy and behavior, they lacked ITO performance characterization and failed to link the high-energy negative ion behavior with the damage of ITO films. In our previous study, it has been verified that the regulation of high-energy negative ions by additional electrodes can effectively inhibit sputtering damage and improve the photoelectric performance of ITO films.[17]

This study leverages electrostatic quadrupole (EQP) plasma diagnostic technology to investigate the mechanistic impact of high-energy negative ion dynamics on sputtering damage in TCO thin films. It explores the influence of power and gas pressure on generation of high-energy oxygen negative ions, elucidates the mechanism of high-energy O^- production, and analyzes the potential effects of high-energy O^- on the growth of ITO thin films. These findings provide essential physical insights to support the optimization of TCO thin film deposition processes and the design of advanced magnetron sputtering target structures.

2. Experiment

In this work, ITO thin films were prepared using the DC magnetron sputtering method, and the experimental device is shown in Fig. 1. The magnetron is positioned to the left of the six-way cross vacuum chamber (with a diameter of 16 cm and a length of 25 cm), and is powered by a direct current power supply (Truplasma DC 4020, Trumpf Huettinger). The target material consists of indium tin oxide (ITO) containing 90% wt.% In_2O_3 and 10% wt.% SnO_2. The EQP plasma analyzer (EQP 1000, Hiden) is mounted on the right flange, a substrate bracket (stainless steel, 80 mm diameter, 5 mm thickness) with an aperture (1 mm diameter) are mounted on the EQP probe, both of which are well grounded. The distance between the target and the EQP probe is fixed at 70 mm. The background vacuum of the chamber before the experiment was less than 1.0×10^{-4} Pa. In this study, the discharge power ranges from 50 W to 200 W, and the pressure varies from 0.4 Pa to 1 Pa.

In terms of film characterization, the crystal structure of ITO films was analyzed by x-ray diffraction (XRD, D8 Advance, Brucker) using θ–2θ mode, and the source was the Cu $K\alpha$ spectral line with wavelength 0.15418 nm. The elemental composition and chemical bond state of the sample surface were analyzed using the ESCALAB 250XI x-ray photoelectron spectrometer (XPS) equipped with an Al K_α ($h\upsilon = 1486.6$ eV) x-ray source and an HeI (21.2 eV) x-ray source. The surface and cross section morphology of the samples were observed by a Hitachi (SU-8010) scanning electron microscope (SEM). The transmittance of the film was measured by SHIMADZU UV-2550 UV-visible spectrophotometer. The wafer resistance of the film was measured using a four-point collinear probe and a Keithley 2400 source meter.

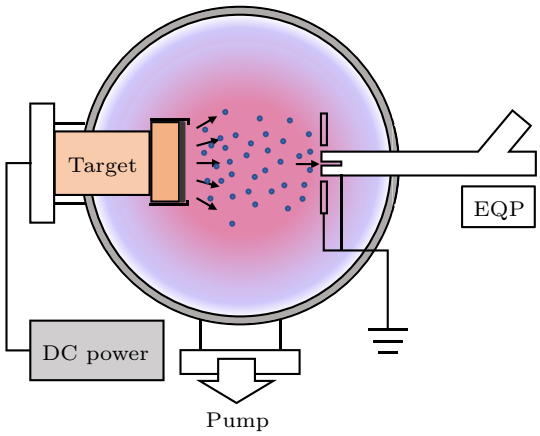


Fig. 1. Schematic diagram of DC magnetron sputtering system at Soochow University.

3. Results and discussion

3.1. Ion behaviors

Figure 2 shows the main mass spectra of (a) positive ions and (b) negative ions in the deposition area obtained by EQP plasma analyzer when the discharge power is 150 W and the air pressure is 6×10^{-1} Pa. It is evident that negative ions dominate the ions incident on the substrate surface, primarily comprising species such as O^-, O_2^-, and InO^-, while positive ions, including Ar^+ and In^+, are relatively scarce.[18] The negative

ion density surpasses that of positive ions by two orders of magnitude. The prevalence of negative ions can be attributed to sputtering from the target material, with its flux closely linked to the sputter rate of the target material. In contrast, positive ions originate from collision ionization processes between electrons and Ar/In atoms. Thus, their flux should be closely associated with electron temperature and density.

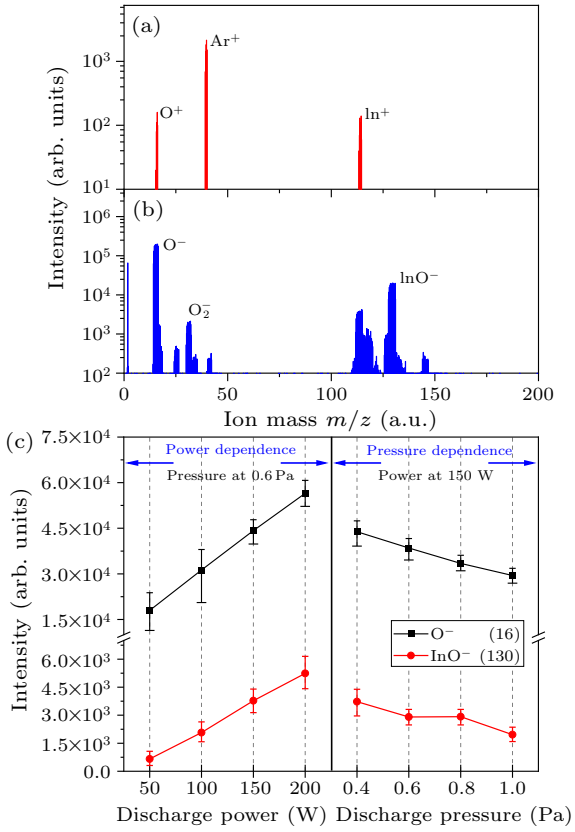


Fig. 2. Mass spectra of the main (a) positive and (b) negative ions incident on the substrate surface. (c) Negative ion concentration at different power and pressure.

In Fig. 2(c), the monitoring of O^- and InO^- ions' information is performed with various power and pressure, which will be advantageous for modulating ion parameters and optimizing deposition process parameters in subsequent steps. It is observable that increasing power enhances the sputter rate of the target material, consequently leading to a substantial augmentation in negative ion flux. Conversely, elevating gas pressure results in a reduction of plasma density within the sputtering zone, suppressing target surface current, and subsequently causing a reduction in negative ion flux.

Figure 3 illustrates the influence of different discharge powers on the energy distribution curves of key positive ions under a discharge pressure of 0.6 Pa. Both Ar^+ and In^+ ions exhibit pronounced energy peaks in the low-energy region, centered at approximately 4 eV. Ar^+ ions predominantly originate from the primary plasma region and undergo acceleration within the substrate sheath layer, where their energy primarily depends on the potential difference across the sheath layer (sheath + pre-sheath). Given that both our substrate and EQP probe are grounded, the sheath potential difference is approximately equal to the plasma potential. Consequently, we calculate the average energy of Ar ions to be around 4 eV, which closely aligns with the plasma potential measured subsequently using probes. In contrast, In^+ ions stem from electron collision ionization of sputtered In atoms within the plasma region. Their energy is slightly higher than that of Ar^+ ions, as it arises not only from sheath acceleration but also from collision sputtering processes involving argon ions. In general, augmenting discharge power elevates plasma potential, consequently resulting in increased ion energy.

Figure 3(c) illustrates the influence of discharge power on the energy distribution of O^- ions incident on the substrate surface. It is evident that the energy distribution of oxygen negative ions exhibits a multi-peak structure.[9,19,20] The high-energy peaks, indicated by spades, primarily originate from high-energy O^- ions sourced from the target surface, accelerated by the cathode sheath layer, with their energy primarily determined by the target voltage ($\sim eV_T$).[21–23] As the power increases, the target voltage increases and the peak value moves to the high energy region. Furthermore, high-energy oxygen molecular ions O_2^-, accelerated by the cathode sheath layer, may undergo dissociation in the primary plasma region, generating oxygen negative ions ($O_2^- \rightarrow O^- + O$).[22] These peaks correspond to ion fragments that retain their attached electrons, and their energy $E_{f,ion}$ can be expressed as[24,25]

$$E_{f,ion} = \frac{m_{f,ion}}{m_M}(-eV_C). \tag{1}$$

Here, $m_{f,ion}$ is the mass of the ion fragment and m_M is the mass of the parent molecule ion. The energy of these O^- ions is approximately half the target voltage ($\sim 0.5V_T$),[26] as denoted by square markers. The low-energy peaks, marked by clubs, could potentially represent some oxygen atoms sputtered in the target pre-sheath region, forming oxygen negative ions by electron attachment,[27] although this theory requires further validation. The low-energy peaks marked by hearts represent those oxygen negative ions that experience a decrease in energy due to non-elastic collisions with neutral particles during their transport to the substrate.

In Fig. 3(d), we examine the influence of different discharge powers on the energy distribution of InO^- ions incident on the substrate surface. It is evident that the energy distribution of InO^- negative ions exhibits distinct high-energy and low-energy peaks. Although the InO^- ion flux is an order of magnitude lower than that of O^- ions, its substantial molecular mass results in non-negligible sputter damage. Likewise, reducing sputtering power can suppress the generation of high-energy InO^- ions.

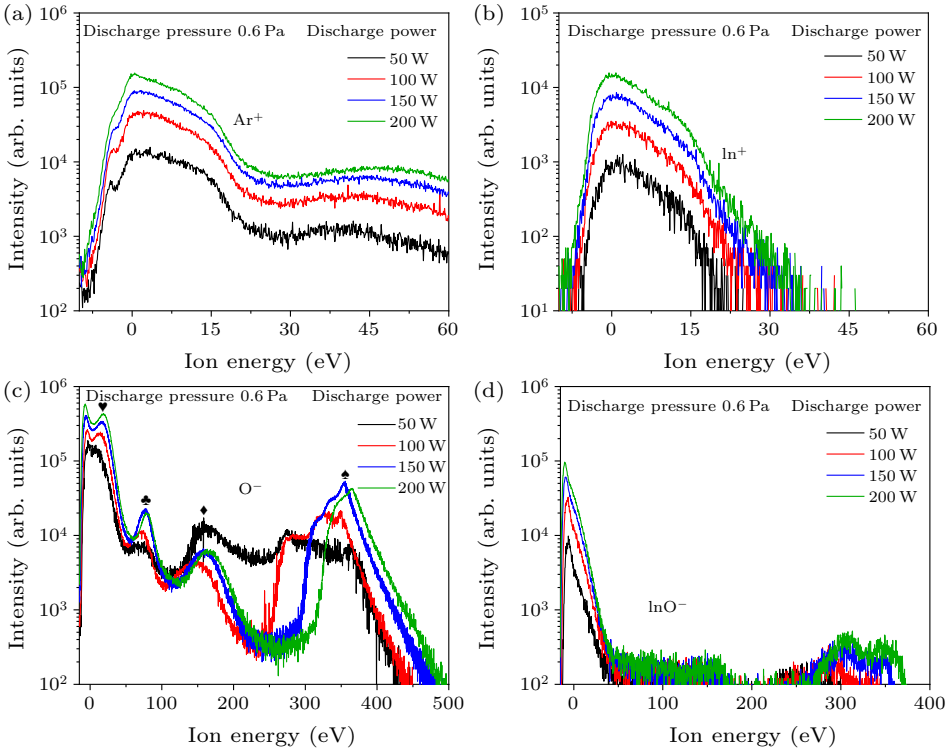


Fig. 3. Effect of discharge power on energy distribution of ions incident on substrate surface: (a) Ar^+, (b) In^+, (c) O^-, (d) InO^-.

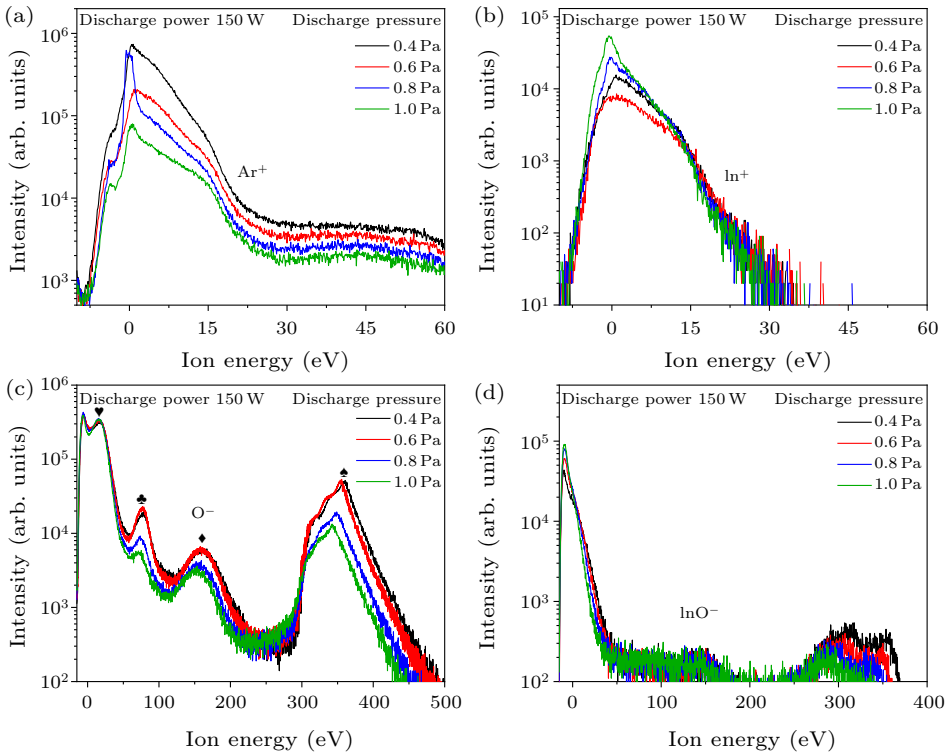


Fig. 4. Effect of discharge pressure on energy distribution of ions incident on substrate surface: (a) Ar^+, (b) In^+, (c) O^-, (d) InO^-.

Figure 4 illustrates the influence of different discharge pressures on the energy distribution curves of key positive and negative ions at 150 W discharge power. In general, the peak position of these four ions did not change under the influence of the change of air pressure, but the peak value and peak width change to some extent. For Ar^+ ion, the peak height becomes 8.0×10^{-5}, the peak width becomes smaller and the peak becomes sharper. Similarly, the peak strength of In^+ ion gradually increases by 8.0×10^{-4} with the increase of air pressure, and the capping becomes sharper. The peak values of O^- and InO^- are not significantly changed by changing the air pressure, and the energy distribution curves of O^- and InO^-

are more similar under different air pressures.

Combined with the energy distribution curves of oxygen negative ions depicted in Figs. 3(c) and 4(c), we can employ the following equations to straightforwardly compute the average energy of high and low-energy oxygen negative ions, along with the proportion of high-energy ions:

$$\bar{E}_{\mathrm{i}} = \frac{\int E \cdot f_{\mathrm{i}}(E)\,\mathrm{d}E}{\int f_{\mathrm{i}}(E)\,\mathrm{d}E}, \tag{2}$$

$$\frac{n_{\mathrm{high}}}{n_{\mathrm{total}}} \approx \frac{\int_{200}^{500} f_{\mathrm{i}}(E)\,\mathrm{d}E}{\int_{0}^{500} f_{\mathrm{i}}(E)\,\mathrm{d}E}, \tag{3}$$

where $f_{\mathrm{i}}(E)$ represents the ion energy distribution function, n_{high} signifies the ion density in the high-energy region, and n_{total} stands for the total ion density.

Figure 5 illustrates variations in the average energy of high-energy and low-energy O^- ions incident on the substrate surface and the proportion of high-energy ion density under different discharge power and gas pressure conditions. The asterisks denote the values of target voltage monitored during the discharge process. It is observable that increasing power typically accompanies an elevation in target voltage, thus enhancing the energy of high-energy O^- ions. Additionally, we observe that high-energy oxygen negative ions tend to be slightly higher than the target voltage because during the sputtering process, incident Ar ions contribute some energy to O^- ions. Increasing gas pressure intensifies collisions between high-energy O^- ions and neutral particles, resulting in a reduction in both high-energy O^- ion energy and their proportion.

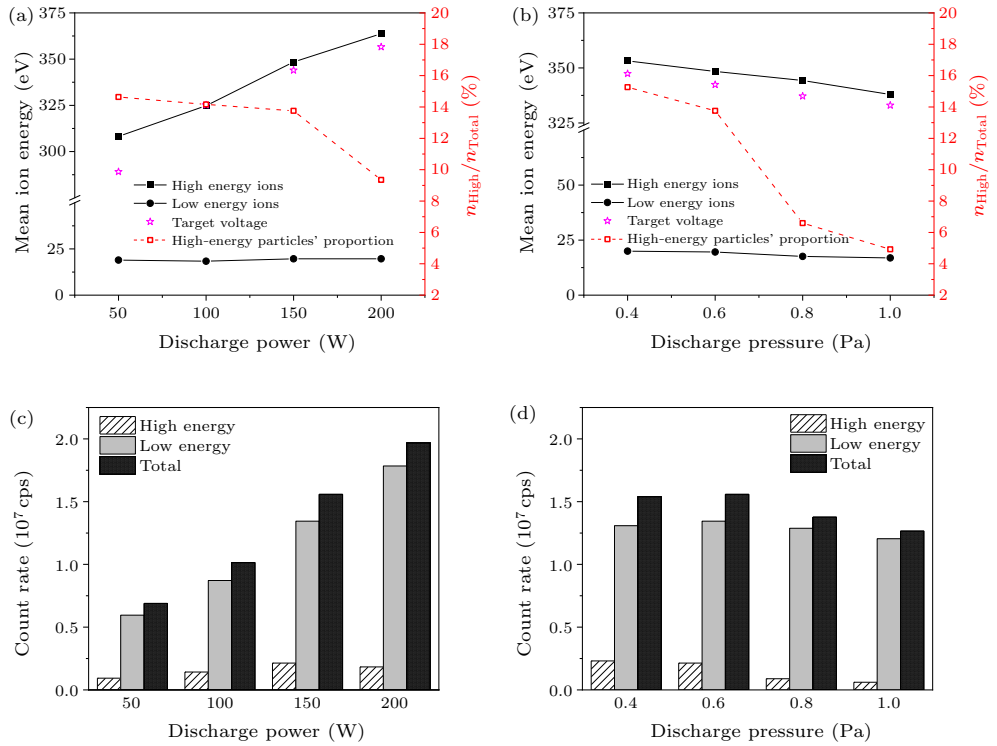


Fig. 5. Effects of discharge power (a) and pressure (b) on the average energy and density ratio of high energy and low energy O^- ions incident on the substrate surface, and effect of discharge power (c) and pressure(d) on high energy and low energy O^- ion fluxes incident on substrate surface.

Surprisingly, we find that increasing power also leads to a decrease in the proportion of high-energy O^- ions. To further investigate the underlying reasons, we systematically analyze the variations in high-energy and low-energy oxygen negative ion flux with discharge power and gas pressure [as depicted in Figs. 5(c) and 5(d)]. It is evident that while increasing power has a minimal impact on the quantity of high-energy oxygen negative ions, it significantly increases the quantity of low-energy oxygen negative ions, consequently reducing the proportion of high-energy oxygen negative ions. Elevating gas pressure partially decreases the quantity of low-energy oxygen negative ions and exhibits a more pronounced inhibitory effect on high-energy oxygen negative ions.

3.2. Film characterizations

Figures 6(a) and 6(b) depict SEM images of the surface morphology of ITO thin films under varying discharge power and gas pressure conditions. The SEM results manifest that, within the current parameter range, augmenting discharge power and Ar flow rate (gas pressure) markedly enhances grain size and crystallinity.[28] The enhancement in film crystalline quality is considerably more pronounced with increased gas pressure than with increased power,[29] owing to the gas pressure elevation's effectiveness in reducing the energy and flux of high-energy oxygen negative ions, thereby averting severe sputter damage to the thin film.

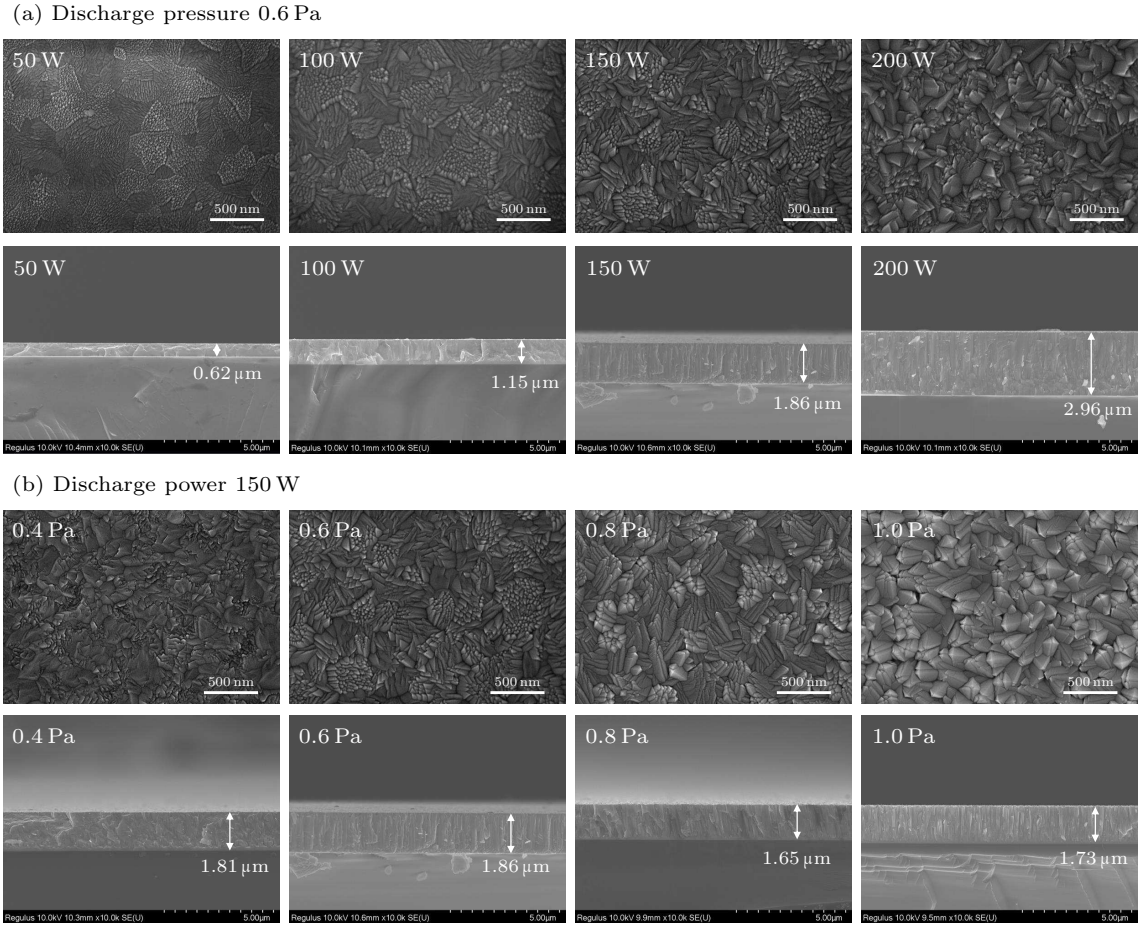


Fig. 6. Surface morphology of ITO film under different discharge power (a) and discharge pressure (b).

From the SEM cross-sectional morphology image, it is evident that we have successfully fabricated a uniform and dense ITO thin film on a Si substrate, with a predominantly columnar crystal growth structure.[30] The thin film growth rate is primarily determined by discharge power, with relatively weaker sensitivity to gas pressure. Therefore, it is difficult to analyze the effect of discharge power on the film resistivity, so this study mainly analyzes the effect of discharge pressure on the film. Under conditions of 150 W and 0.6 Pa, the growth rate measures 62 nm/min. Subsequent studies can try to increase the discharge power (above 150 W) and gas pressure to obtain better film forming quality.

Figure 7 depicts x-ray photoelectron spectroscopy (XPS) of the thin film under typical discharge conditions (power: 150 W, pressure: 0.6 Pa). The O 1s spectra show that the main peak (O I) at 529.7 eV belongs to the In–O–In oxygen bond, and the other peak (O Ⅱ) at 531.4 eV belongs to the O vacancy in the In_2O_3 matrix, indicating that there is oxygen vacancy (In_2O_{3-x}) on the surface of the film.[31,32] This observation aligns, to a considerable extent, with the x-ray diffraction (XRD) results, affirming that oxygen vacancy formation is closely associated with the near-target oxygen-depleted environment during the magnetron sputtering process.

Figure 8 illustrates x-ray diffraction patterns (θ–2θ scan) as a function of discharge power and gas pressure. XRD film phase analysis reveals that the film primarily comprises the (400) phase,[33] indicating that the stoichiometric percentage of O and In is less than 1.5, with a significant presence of oxygen vacancies within the film. Generally, a smaller peak intensity ratio between the (222) peak and the (400) peak implies a lower elemental stoichiometric ratio of O and In in the film, resulting in reduced film transparency but higher crystallinity.[34] To mitigate oxygen vacancies, it is advisable to introduce increased oxygen in later experiments. Furthermore, we observed that in the edge region of the film deposition, the ratio of the (222) peak to the (400) peak is higher, indicating a reduced presence of oxygen vacancies in the film. This observation reflects distinct spatial distributions of In and O particles sputtered by the circular planar target, resulting in varying elemental stoichiometric ratios in films deposited in different regions.[35]

Table 1 lists the average light transmittance of the ITO film within the wavelength range of 400–800 nm and the corresponding optical bandgap parameters at different pressures, according to the UV-visible spectra of ITO film deposited under different pressures shown in Fig. 9. A notable rise in the average light transmittance is evident with increasing pressure. As the pressure increases, the collision frequency rises, lead-

ing to enhanced scattering of argon ions. Consequently, the energy of argon ions striking the target diminishes. Additionally, the heightened collision frequency results in the dissipation of energy by high-energy O ions enroute to the substrate. With minimized sputtering damage, crystal grains deposited on the substrate effortlessly amalgamate into larger, more cohesive structures. Another contributing factor is that as the sputtering pressure increases, the band gap of the film shifts its absorption edge towards the blue spectrum, consequently augmenting its average transmittance.

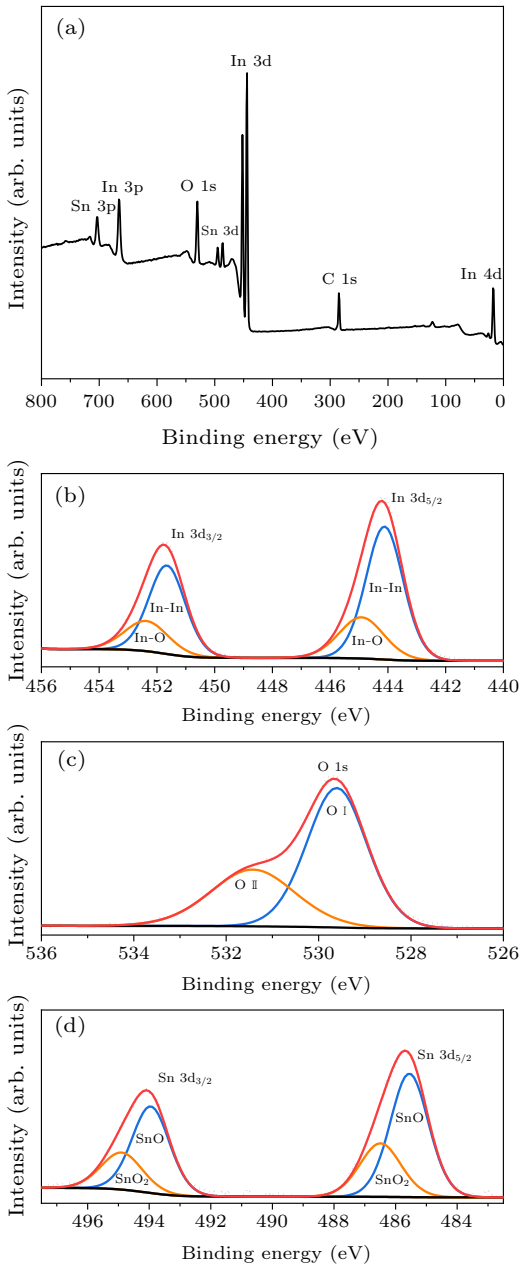


Fig. 7. XPS spectra of thin films under typical discharge parameters (discharge power 150 W, discharge pressure 0.6 Pa).

It has been observed that resistivity notably decreases with increasing pressure, particularly within the range of 0.4–0.8 Pa, where the decline is particularly rapid. This phenomenon can be attributed to variations in the sputtering chamber's Ar^+ ion number density and collision frequency at different pressure levels. With increasing pressures, the decreasing energy and flux of high-energy O^- ions facilitate the deposition of ITO target atoms and atomic groups onto the substrate. Consequently, films exhibit higher migration energy, superior crystal quality, larger grain sizes, fewer grain boundaries, and enhanced carrier mobility. However, as pressure exceeds 0.8 Pa, despite the increase in carrier mobility due to reduced grain boundaries, looser crystal grains limit carrier mobility. This equilibrium between grain boundary effects and crystal grain density explains the stabilization of resistivity changes at pressures exceeding 0.8 Pa.

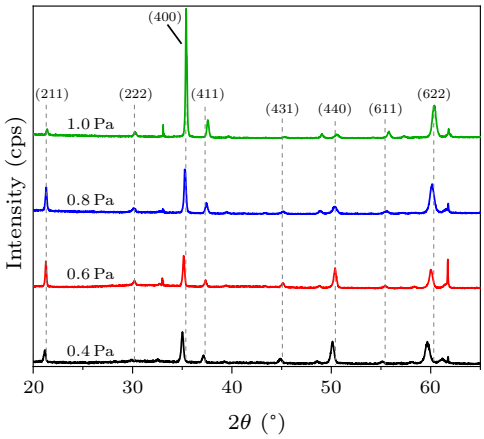


Fig. 8. XRD lines of ITO films under different discharge power and pressure conditions.

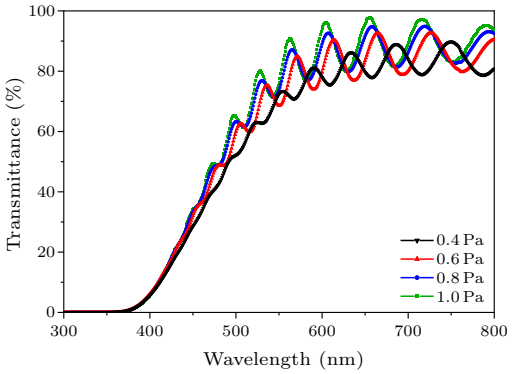


Fig. 9. Ultraviolet-visible spectra of ITO films deposited under different pressures.

Table 1. Changes of key photoelectric characteristics with discharge pressure.

Pressure (Pa)	Transmittance (%)	Band gap (eV)	Resistivity (Ω·cm)
0.4	52.6	3.19	0.48
0.6	54.9	3.32	0.36
0.8	57.0	3.33	0.24
1.0	58.1	3.34	0.23

4. Summary and conclusion

In this study, ITO films were deposited onto silicon and quartz substrates using the magnetron sputtering technique in a pure argon environment. The investigation focuses on the influence of discharge power and discharge pressure on the ion

flux and energy distribution function incident upon the substrate surface.

The energy distribution of oxygen anion shows a multi-peak structure. The high energy peaks are mainly derived from the high energy O^- ions of the target surface, which are accelerated by the cathode sheath of the target surface, and the energy is mainly dependent on the target voltage ($\sim eV_T$). In addition, the high-energy oxygen molecular ion O_2^- accelerated by the cathode sheath may dissociate in the main plasma region, producing oxygen negative ions ($O_2^- \rightarrow O^- + O$), the energy of this part of the O^- ion is approximately equal to half of the target voltage ($\sim 0.5eV_T$). The low energy peak may be a part of the sputtered oxygen atoms in the target pre-sheath region, combined with electrons to produce oxygen ions. Nevertheless, this theory still needs further verification. The lowest energy low energy peak is the part of the substrate in the process of transport to the neutral particles and inelastic collision, resulting in energy reduction of the oxygen anion.

The energy and flux of high and low energy oxygen anions can be adjusted by changing the discharge power and discharge pressure. The target voltage usually increases as the discharge power increases, resulting in an increase in the energy of high-energy O^- ions and an increase in the number of O^- ions. This increase has a negligible effect on the number of high-energy negative oxygen ions, but significantly increases the number of low-energy O^- ions, thereby reducing the proportion of high-energy O^- ions. Increasing the air pressure increases the collision frequency between high energy O^- ions and neutral particles, reduces the energy of high energy O^- ions and their number, and can better inhibit the sputtering damage of high energy O^- ions on the film. Therefore, it is suggested to reduce the sputtering power, increase the air pressure, inhibit the production of high energy O^- ions, and improve the quality of the film in the follow-up study.

Acknowledgments

This work was supported by the National Key R&D Program of China (Grant No. 2022YFE03050001) and the National Natural Science Foundation of China (Grant Nos. 12175160 and 12305284). The authors thank Suzhou Maxwell Technologies Co., Ltd. for partial hardware and particle financial support to carry out the research.

References

[1] Haschke J, Dupré O, Boccard M and Ballif C 2018 *Solar Energy Mater. Solar Cells* **187** 140
[2] Shen W Z, Zhao Y X and Liu F 2022 *Front. Energy* **17** 9
[3] Chavan G T, Kim Y, Khokhar M Q, Hussain S Q, Cho E C, Yi J, Ahmad Z, Rosaiah P and Jeon C W 2023 *Nanomaterials* **13** 1226
[4] Nunomura S, Sakata I and Matsubara K 2018 *Phys. Rev. Appl.* **10** 054006
[5] Le A H T, Dao V A, Pham D P, Kim S, Dutta S, Thi Nguyen C P, Lee Y, Kim Y and Yi J 2019 *Solar Energy Mater. Solar Cells* **192** 36
[6] Liu K, Chen B, Yu Z S J, Wu Y L, Huang Z T, Jia X H, Li C, Spronk D, Wang Z J, Wang Z G, Qu S C, Holman Z C and Huang J S 2022 *J. Mater. Chem. A* **10** 1343
[7] Linss V, Bivour M, Iwata H and Ortner K 2019 *AIP Conf. Proc.* **2147** 040009
[8] Macias-Montero M, Garcia-Garcia F J, Álvarez R, Gil-Rostra J, González J C, Cotrino J, Gonzalez-Elipe A R and Palmero A 2012 *J. Appl. Phys.* **111** 054312
[9] Mráz S and Schneider J M 2006 *J. Appl. Phys.* **100** 023503
[10] Street R, Biegelsen D and Stuke J 1979 *Philos. Mag. B* **40** 451
[11] Ishibashi S, Higuchi Y, Ota Y and Nakamura K 1990 *J. Vac. Sci. Technol. A* **8** 1403
[12] Konishi T and Ohdaira K 2017 *Thin Solid Films* **635** 73
[13] Caudevilla D, García-Hemme E, San Andrés E, Pérez-Zenteno F, Torres I, Barrio R, García-Hernansanz R, Algaidy S, Olea J, Pastor D and del Prado A 2022 *Mater. Sci. Semiconduct. Process.* **137** 106189
[14] Tominaga K, Iwamura S, Fujita I, Shintani Y and Tada O 1982 *Jpn. J. Appl. Phys.* **21** 999
[15] Mráz S and Schneider J M 2006 *Appl. Phys. Lett.* **89** 051502
[16] Welzel T and Ellmer K 2011 *Surf. Coat. Technol.* **205** S294
[17] Huang T, Mo C, Cui M, Li M, Ji P, Tan H, Zhang X, Zhuge L and Wu X 2024 *Vacuum* **221** 112848
[18] Pokorny P, Miýina M, Bulíř J, Lančok J, Fitl P, Musil J and Novotny M 2011 *Plasma Process. Polym.* **8** 459
[19] Welzel T, Naumov S and Ellmer K 2011 *J. Appl. Phys.* **109** 073302
[20] Mahieu S, Leroy W P, Van Aeken K and Depla D 2009 *J. Appl. Phys.* **106** 093302
[21] Seeger S, Harbauer K and Ellmer K 2009 *J. Appl. Phys.* **105** 053305
[22] Zeuner M, Neumann H, Zalman J and Biederman H 1998 *J. Appl. Phys.* **83** 5083
[23] Tominaga K and Kikuma T 2001 *J. Vac. Sci. Technol. A* **19** 1582
[24] Welzel T and Ellmer K 2012 *J. Vac. Sci. Technol. A* **30** 061306
[25] Bowes M, Poolcharuansin P and Bradley J W 2013 *J. Phys. D: Appl. Phys.* **46** 045204
[26] Mišina M, Bradley J W, Bäcker H, Aranda-Gonzalvo Y, Karkari S K and Forder D 2002 *Vacuum* **68** 171
[27] Lee C and Lieberman M A 1995 *J. Vac. Sci. Technol. A* **13** 368
[28] Huang M, Hameiri Z, Aberle A G and Mueller T 2015 *Vacuum* **121** 187
[29] Lei H, Ichikawa K, Hoshi Y, Wang M, Uchida T and Sawada Y 2010 *Thin Solid Films* **518** 2926
[30] Zhao M J, Zhang J F, Huang Q H, Wu W Y, Tseng M C, Lien S Y and Zhu W Z 2022 *Vacuum* **196** 110762
[31] Gan J, Lu X, Wu J, Xie S, Zhai T, Yu M, Zhang Z, Mao Y, Wang S C I, Shen Y and Tong Y 2013 *Sci. Rep.* **3** 1021
[32] Lei F, Sun Y, Liu K, Gao S, Liang L, Pan B and Xie Y 2014 *J. Am. Chem. Soc.* **136** 6826
[33] Zhao L, Zhou Z, Peng H and Cui R 2005 *Appl. Surf. Sci.* **252** 385
[34] Sezemsky P, Burnat D, Kratochvil J, Wulff H, Kruth A, Lechowicz K, Janik M, Bogdanowicz R, Cada M, Hubicka Z, Niedziałkowski P, Białobrzeska W, Stranak V and Śmietana M 2021 *Sens. Actuators B* **343** 130173
[35] Huang M, Liu Y S, He Z B and Yi Y 2022 *Chin. Phys. B* **31** 066101